Spectral filtering in pulsed photothermal temperature profiling of collagen tissue phantoms

Matija Milanič
Boris Majaron
Jožef Stefan Institute
Complex Matter Department
Jamova 39
Ljubljana, Slovenia SI-1000

Abstract. We present an experimental comparison of pulsed photothermal (PPT) profiling in collagen-based tissue phantoms utilizing different midinfrared spectral bands. Laser-induced temperature profiles are reconstructed using a custom optimization code within the customary monochromatic approximation. Both experimental results and a detailed numerical simulation of the procedure demonstrate that, despite the associated reduction of signal-to-noise ratio, appropriate spectral filtering reduces the broadening of temperature peaks and thus improves the accuracy of temperature profiling. For our experimental system, best performance is obtained when applying a long-pass filter with cut-on wavelength at $3.4-3.8$ μm. Because our collagen gel mimics infrared and thermal properties of human skin, we believe that this conclusion is transferrable to PPT radiometric profiling of human skin *in vivo*. © *2009 Society of Photo-Optical Instrumentation Engineers.* [DOI: 10.1117/1.3275465]

1 Introduction

Photothermal radiometry utilizes time-resolved measurements of infrared (IR) emission upon laser irradiation to determine specific information about the sample. For example, a temperature depth profile induced by a laser pulse can be reconstructed if optical and thermal properties of the sample are known.[1] Such pulsed photothermal radiometric (PPTR) temperature profiling allows noninvasive determination of chromophore distribution and specific heating in human skin,[2,3] with important implications for dermatologic laser therapy.[4,5]

PPTR was found to be very effective in determining the depth of isolated subsurface absorbers in optically scattering tissues.[3,6,7] On the other hand, this approach is notorious for inherent broadening of distinct temperature peaks, which increases rapidly with object depth.[6–8] We believe that this effect may, in part, arise from incompatibility between the broadband acquisition of IR radiation and the monochromatic approximation, commonly applied to reduce computational complexity of the profile reconstruction process. This holds, in particular, for soft biological tissues, which feature a pronounced variation of absorption coefficient $\mu(\lambda)$ in the relevant mid-IR spectral range. A recent study has confirmed that appropriate narrowing of the acquisition spectral band improves the accuracy of PPTR profiling in layered agar samples, despite the related decrease of signal-to-noise ratio (SNR).[9]

Herein, we present a similar study of PPTR temperature profiling in collagen gel tissue phantoms, with optical and thermal properties resembling those of human skin. The pro-filing performance when using the customary spectral band of the InSb radiation detector ($\lambda=3.0-5.6$ μm) is compared against spectral bands narrowed by three long-pass filters. The effective IR absorption coefficient values (μ_{eff}) used in the reconstruction process are determined separately for each spectral band.[10]

Our experimental observations are supported by a detailed numerical simulation of the procedure. For initial temperature profiles, resembling those in our collagen samples, we compute PPTR signals for several acquisition spectral bands and augment them with noise that is consistent with our experimental system. By varying the lower wavelength limit between 3.0 and 5.0 μm, we can determine the optimal amount of spectral filtering. The analysis is also extended to a more complex temperature profile, such as could be found in laser irradiation of port wine stain lesion *in vivo*.

2 Theoretical Background

Fundamentals of PPTR temperature profiling can be found elsewhere.[3,6,11] Expression for the transient part of a radiometric signal, $\Delta s(t)$, is derived by linearization of Planck' law of radiation around the baseline skin temperature T_b. In a most general form, $\Delta s(t)$ is thus related to temperature rise in the sample $\Delta T(z,t)$ as[7,10,11]

$$\Delta s(t) = C\varepsilon A \sin^2\theta \int_{\lambda_l}^{\lambda_h} R(\lambda)B'_\lambda(T_b)\mu(\lambda)$$

$$\times \int_{z=0}^{\infty} \Delta T(z,t)e^{-\mu(\lambda)z}\mathrm{d}z\mathrm{d}\lambda, \qquad (1)$$

Address all correspondence to: Matija Milanič, Jožef Stefan Institute, Complex Matter Department, Jamova 39, Ljubljana, Slovenia SI-1000. Tel: 00386-1-477-3208; Fax: 00386-1-423-5400; E-mail: matija.milanic@ijs.si

where ε is sample emissivity, λ_l and λ_h define the acquisition spectral band, $\mu(\lambda)$ is sample IR absorption coefficient, and $B'_\lambda(T_b)$ denotes the temperature derivative of Planck's radiation formula. The radiation detector is characterized by its active area A, half-angle of field of view θ, and spectral responsivity $R(\lambda)$. Constant C accounts for other experimental factors, such as losses in collection optics, etc.

By expressing $\Delta T(z,t)$ after pulsed laser irradiation as a convolution of the initial temperature profile $\Delta T(z,0)$ and Green's function solution to the one-dimensional heat diffusion equation, Eq. (1) can be rewritten as

$$\Delta s(t) = C\varepsilon A \sin^2\theta \int_{\lambda_l}^{\lambda_h} R(\lambda)B'_\lambda(T_b) \int_{z=0}^{\infty} \kappa_\lambda(z,t)\Delta T(z,0)\mathrm{d}z\mathrm{d}\lambda.$$

(2)

In the following, we apply the monochromatic kernel function $\kappa_\lambda(z,t)$ as derived by Milner[3] for a semi-infinite medium and convective and/or radiative heat transfer at the surface.

Prior to signal analysis, it is customary to calibrate the system by fitting radiometric signal values obtained from a blackbody with varying temperature to Planck's radiation formula. Performing such calibration removes most of the error associated with linearization of Planck's radiation law in Eq. (1) and eliminates experimentally specific prefactors C, ε, A, and θ, enabling absolute measurements of temperature rise in the sample.[7,12]

Calibrated PPTR signals $\Delta S(t)$ thus assume a form

$$\Delta S(t) = \int_{z=0}^{\infty} K(z,t)\Delta T(z,0)\mathrm{d}z,$$

(3)

where the kernel function $K(z,t)$ equals $\kappa_\lambda(z,t)$ in the case of monochromatic radiation detection.

Experimental PPTR signals are represented by vectors $\mathbf{S}$ with components $S_i = \Delta S(t_i)$. Hence, Eq. (3) becomes multiplication of the initial temperature profile, $\mathbf{T}$ $[T_j = \Delta T(z_j)]$, with a kernel matrix $\mathbf{K}$ $[K_{i,j} = K(z_i,t_j)\Delta z]$

$$\mathbf{S} = \mathbf{KT}.$$

(4)

Nevertheless, reconstruction of $\mathbf{T}$ from experimental signal $\mathbf{S}$ presents a severely ill-posed problem, generally with no exact solution.[3] The best approximate solution is most commonly obtained by iterative minimization of residual norm $\|\mathbf{S}-\mathbf{KT}\|^2$.

3 Tissue Phantom Experiments

3.1 Materials and Methods

3.1.1 Collagen gel tissue phantoms

Our tissue phantoms consist of a ~ 2-mm-thick collagen gel substrate layer, one optically absorbing layer, and a superficial collagen layer with controlled thickness (Fig. 1). Collagen gel was prepared by dissolving 1.25 g of collagen powder (bovine skin, Sigma-Aldrich, St. Louis, Missouri) in 6 mL of water with 0.2% of formaldehyde. Polymerization was initiated by heating the mixture to 40 °C in an ultrasound bath, which minimized formation of air bubbles. When the gelatin powder was completely dissolved, each gel layer was pro-
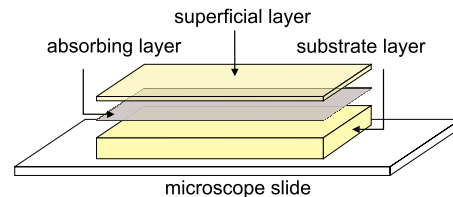
Fig. 1 Schematic of a tissue phantom, consisting of a thin absorbing layer between two gel layers.

duced separately by injecting a suitable amount of the gel solution onto a microscope slide with two identical spacers positioned near each end. A second slide was then placed on top of the setting gelatin layer and pressed against the spacers. Both microscope slides were covered with a Teflon tape to prevent sticking of collagen to the glass surface. When polymerization was complete, the top slide was carefully removed, exposing a gel layer with a flat, smooth surface and uniform thickness.

The absorbing layer consists of a very thin (~ 10-μm), lightly colored (pink) polyethylene foil, which ensures a spatially uniform and repeatable absorption of laser light. By varying the superficial layer thickness, the absorbing layer was positioned at subsurface depths of approximately 0.08, 0.13, 0.22, 0.33, or 0.50 mm (in samples A, B, C, D, and E, respectively). The samples were constructed in a water bath to avoid trapping of air bubbles between adjacent layers.

3.1.2 Experimental setup

Each PPTR measurement involves sample irradiation with a single 1-ms pulse from an Nd:YAG/KTP laser at 532 nm. IR radiation emitted from the center of irradiated area is collected by two planoconvex Si lenses (Galvoptics, Essex, United Kingdom) positioned for magnification $M=1$. The lenses are coated for high transmittance ($T \geq 98\%$) in the acquisition spectral band of the InSb radiation detector (P5968-100, Hamamatsu; $\lambda = 3.0-5.6$ μm) with a 1-mm-diam, 45-deg field of view, and peak spectral sensitivity $R_p = 2.5$ A/W at $\lambda_p = 5.3$ μm [Fig. 2(a)].

On each test site, two radiometric signals were acquired first utilizing the entire spectral band of the IR detector, and then with either one of two long-pass filters inserted between the two condenser lenses. Transmission characteristics $T(\lambda)$ of the two filters (Barr Associates, Westford, Massachusetts) with nominal cut-on wavelengths of 3.77 and 5.03 μm are plotted in Fig. 2(b) (solid and dashed lines, respectively). In addition, the second filter was placed between the second Si lens and detector. Effective spectral transmissivity for this case, calculated by accounting for oblique incidence of IR rays within the detector field of view using the customary relation for interference filters,[13] has a cut-on wavelength of 4.80 μm [Fig. 2(b), dashed-dotted line].

The radiometric signals were acquired for 1.0 s after the laser pulse, at a rate of 50,000 s^{-1}. Transient PPTR signals $\mathbf{S}$ were then obtained by calibrating the raw data using a computer-controlled blackbody (BB701, Omega Engineering, Stamford, Connecticut), subtracting the baseline value and averaging 25 subsequent data points to reduce the sampling rate to more manageable 2000 s^{-1}.
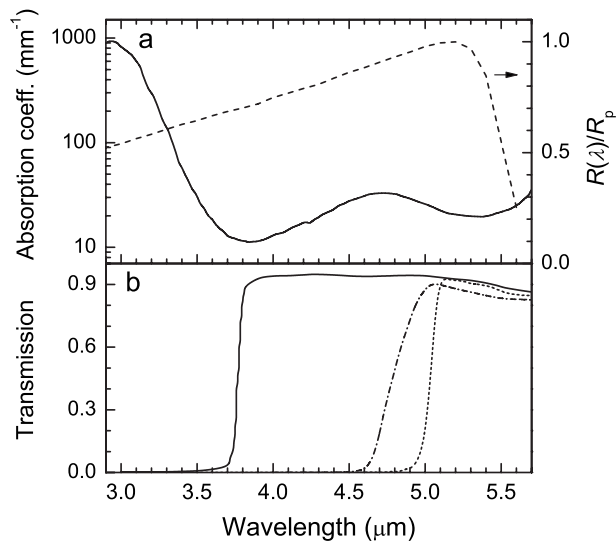
Fig. 2 Absorption coefficient of collagen gel in the mid-IR spectral region (solid line) and spectral responsivity of the InSb detector (relative to its peak value R_p; dashed line). (b) Transmission $T(\lambda)$ of long-pass filters with nominal cut-on wavelengths of 3.77 μm (solid line), 4.80 μm (dashed-dotted line), and 5.03 μm (short dashed line).

Fig. 3 PPTR signals acquired from the same test site in collagen gel sample C with absorbing layer at subsurface depth $z_0 \approx 0.22$ mm using spectral bands with λ_l from 3.0 μm to 5.0 μm.

3.1.3 Reconstruction of temperature profiles

The initial temperature profiles T were reconstructed within the customary monochromatic approximation. Elements of the monochromatic kernel matrix $K = \kappa_\lambda$ were calculated for assumed tissue thermal diffusivity $D = 0.11$ mm^2/s and reduced heat transfer coefficient $h = 0.02$ mm^{-1}. The effective absorption coefficient μ_{eff} was determined separately for each acquisition spectral band following a recently developed analytical approach,[10] taking into account IR spectral properties of the sample, radiation detector, and each cut-on filter (Fig. 2). The obtained values vary from $\mu_{eff} = 21.1$ mm^{-1} at $\lambda_l = 5.0$ μm to 23.0 mm^{-1} for $\lambda_l = 3.0$ μm (see, later, Fig. 6).

The resulting temperature profiles, obtained using a custom implementation of the projected ν-method,[12] consist of 200 equidistant temperature values over a depth range of 1 mm.

3.2 Experimental Results

Figure 3 presents PPTR signals acquired from the same location in sample C using all four spectral acquisition bands. Evidently, experimental noise increases with narrowing of the spectral band. Noise-equivalent (NE) temperature rise, computed as standard deviation of radiometric signal values before laser exposure, amounts to NEΔT = 3.0, 3.4, 6.8, and 8.6 mK for spectral bands with lower limit wavelengths $\lambda_l = 3.0$, 3.8, 4.8, and 5.0 μm, respectively.

In Fig. 4, we compare temperature profiles reconstructed from PPTR measurements on the same sample site using different spectral bands. For sample B [Fig. 4(a)] locations of temperature peaks indicate the absorber depth around 0.13 mm. Temperature profiles obtained using the broad spectral bands ($\lambda_l = 3.0$ and 3.8 μm) are significantly narrower as compared to the narrower spectral bands ($\lambda_l = 4.8$ and 5.0 μm). For sample C with a deeper absorbing layer [Fig.
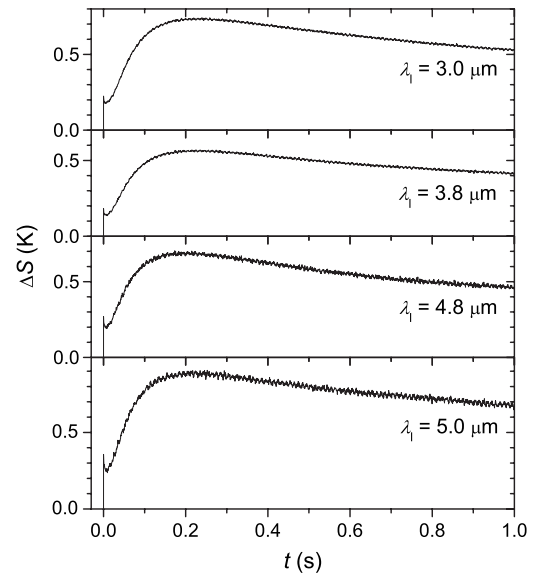
4(b)], the spectral band with $\lambda_l = 3.8$ μm clearly yields the narrowest profiles. However, only the results for $\lambda_l = 4.8$ μm do not include an artifact at the deep end.

Full widths at half maximum (W) of the reconstructed temperature peaks are presented in Fig. 5 for all test samples and spectral bands. For samples A and B, similar widths are obtained at $\lambda_l = 3.0$ and 3.8 μm ($W = 45 - 50$ μm and $W = 65 - 70$ μm for samples A and B, respectively), while the narrower spectral bands result in significantly wider lobes. For samples C and D, the smallest widths are obtained at $\lambda_l = 3.8$ μm ($W = 100 - 105$ μm and $W = 150$ μm, respectively). In test sample E, with the absorbing layer located at depth of $\sim$0.5 mm, the width of reconstructed temperature profile increases monotonically with spectral narrowing.

4 Numerical Simulation

4.1 Simulation Setup

Theoretical PPTR signals (imitating a sampling rate of 50,000 s^{-1} over a 1-s acquisition time) are calculated from assumed initial temperature profiles as $S_0 = KT_0$. To account for spectrally broad radiation detection, we compute the elements of spectrally composite kernel matrix K by dividing the acquisition spectral band into intervals of width 0.02 μm and adding their respective contributions[9,12]

$$K_{i,j} = \frac{\sum_{n=1}^{N} T(\lambda_n) R(\lambda_n) B'_{\lambda_n}(T_b) \kappa_n(z_j, t_i; \mu_n)}{\sum_n T(\lambda_n) R(\lambda_n) B'_{\lambda_n}(T_b)}, \quad (5)$$

where λ_n marks the central wavelength of the n'th spectral interval and μ_n is the corresponding absorption coefficient of the collagen gel. For a more complete data set, we consider—in addition to the four spectral bands used in
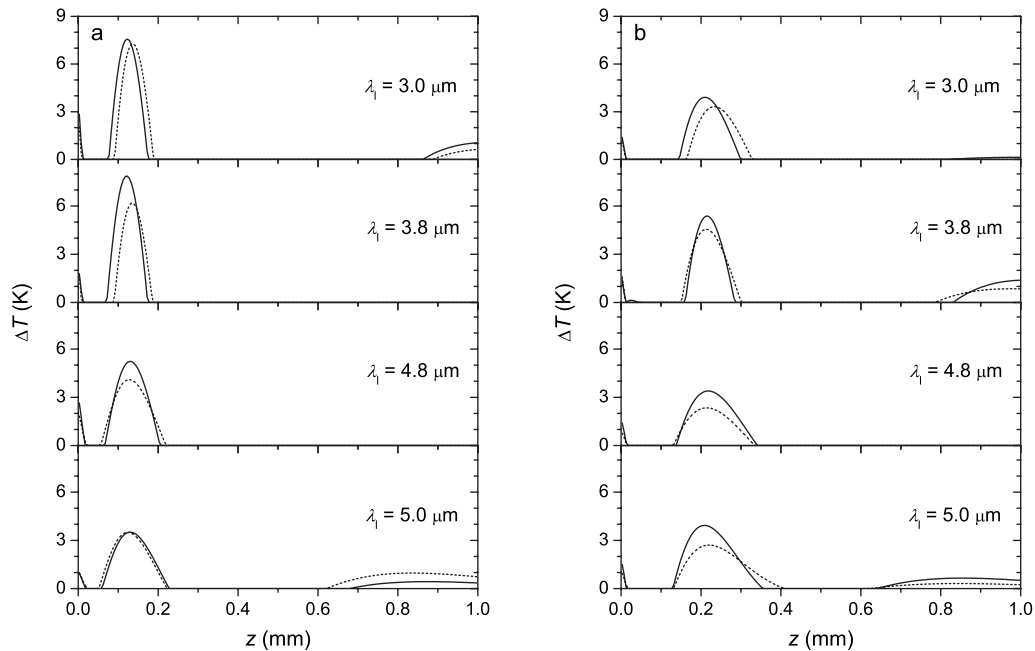
Fig. 4 Reconstructed temperature profiles in (a) sample B and (b) sample C, obtained using four spectral bands. Two results are plotted for each example (solid and dashed line, respectively).

experiments—two spectral bands with a sharp cut-on at $\lambda_l = 3.4$ and 4.3 μm, respectively.

For additional realism, we augment signals S_0 with both zero-mean white noise and so-called $1/f$ noise. We apply the experimentally determined NEΔT values and calculate the corresponding values for the two additional bands (Fig. 6, open circles).[9] On the basis of the analysis of experimental signals, the $1/f$ noise is characterized by corner frequency $f_c = 15$ Hz and exponent $\alpha = 1.3$.[7,14]

Just as in the experimental part, simulated PPTR signals are computationally reduced to 2000 data points ($f = 2000$ s^{-1}). Temperature profiles are then reconstructed using the effective absorption coefficient values μ_{eff}, calculated separately for each spectral band (Fig. 6, solid circles). These values were determined from IR spectral properties of the sample and radiation detector (Fig. 2) by following a recently presented analytical approach.[10] For each test object and spectral band, the reconstruction process is repeated 30 times with different realizations of noise, and the results are statistically analyzed.

4.2 Collagen Tissue Phantoms

For simulation of our experiments in collagen tissue phantoms, we consider initial temperature profiles with a so-called hyper-Gaussian form: $\Delta T(z,0) = \Delta T_0 \exp[-2(z-z_0)^4/w_0^4]$. A good match with experimental data is obtained at parameter values $\Delta T_0 = 10$ K, $w_0 = 26$ μm, and z_0 of 0.08, 0.13, 0.22, 0.33, or 0.53 μm (test objects A–E, respectively).

Figure 7 presents temperature profiles reconstructed from simulated PPTR signals for test objects B and C. Standard deviations of temperature values computed from 30 reconstructions with different noise realizations (indicated by vertical bars) are rather small and thus barely discernible in Fig. 7. For both test objects, spectral bands with $\lambda_l = 3.4$ and
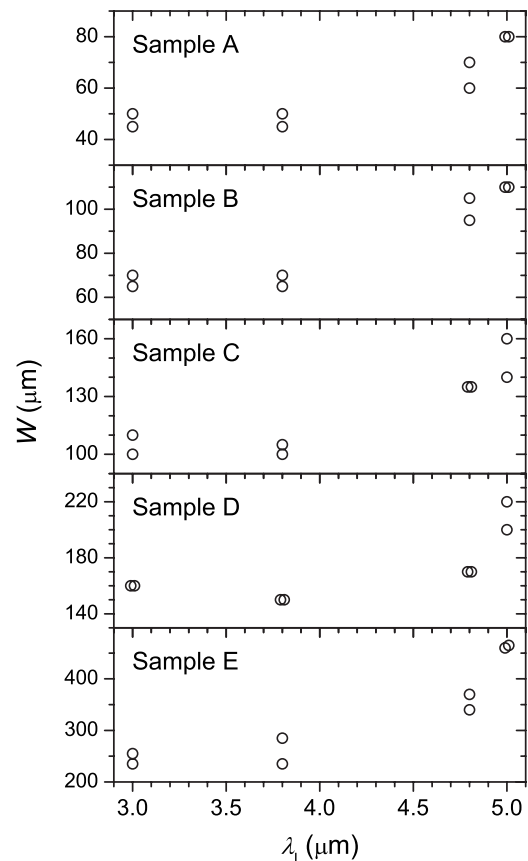
Fig. 5 FWHM widths of the reconstructed temperature peaks in collagen test samples A–E as a function of the lower wavelength limit λ_l. Results from two measurements are presented for each case. The absorbing layers in samples A–E were located at subsurface depths of approximately 0.08, 0.13, 0.22, 0.33, and 0.50 mm, respectively.
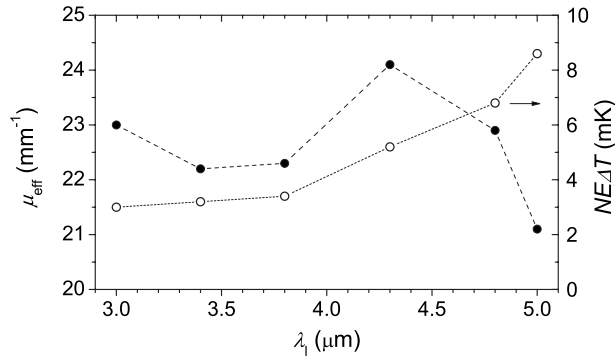
Fig. 6 Effective absorption coefficients, μ_{eff} (solid circles) and noise-equivalent temperature rise, NEΔT (open circles) for acquisition spectral bands with λ_1 between 3.0 and 5.0 μm.

3.8 μm provide more accurate images of the actual temperature profile (thinner line) as compared to the narrower or wider spectral bands.

As seen in Fig. 8, the reconstructed temperature peaks are usually broader than the actual test object ($W = 40$ μm; indicated by dashed line). For object A, the results obtained with λ_1 from 3.0 to 3.8 μm match the actual object width. For objects B–D, minimal widths are obtained at $\lambda_1 = 3.4$ or 3.8 μm, indicating that spectral filtering can improve the ac-

curacy of PPTR temperature profiling. The optimal values amount to 46, 74, and 114 μm for objects B, C, and D, respectively. This conforms to the general rule that broadening of temperature peaks increases roughly proportionally with their depth.[6,8,12] For test object E, the lowest W is obtained at $\lambda_1 = 3.0$ μm, but the minimum is not very distinct.

Because the actual temperature profiles T_0 are known, we can assess also the relative image error, defined as

$$\delta = \frac{\|T - T_0\|}{\|T_0\|}. \tag{6}$$

Figure 9 presents relative image errors δ [Eq. (6)] as a function of λ_1 for all test objects. For object A, the minimal error is obtained at $\lambda_1 = 3.8$ μm ($\delta = 0.07$). For λ_1 above 4.0 μm, δ increases due to decreasing SNR, up to $\delta = 0.38$ at $\lambda_1 = 5.0$ μm. On the other hand, the image error also increases with broadening of the spectral band (reaching $\delta = 0.11$ at $\lambda_1 = 3.0$ μm) due to increasing deficiency of the monochromatic approximation.

A similar trend is observed for object B (Fig. 9), with a distinct optimum at $\lambda_1 = 3.4$ μm ($\delta = 0.17$) and higher image errors for both broader and narrower spectral bands. With increasing depth of the simulated absorption layer, the image errors increase and selection of the acquisition spectral band becomes less critical.
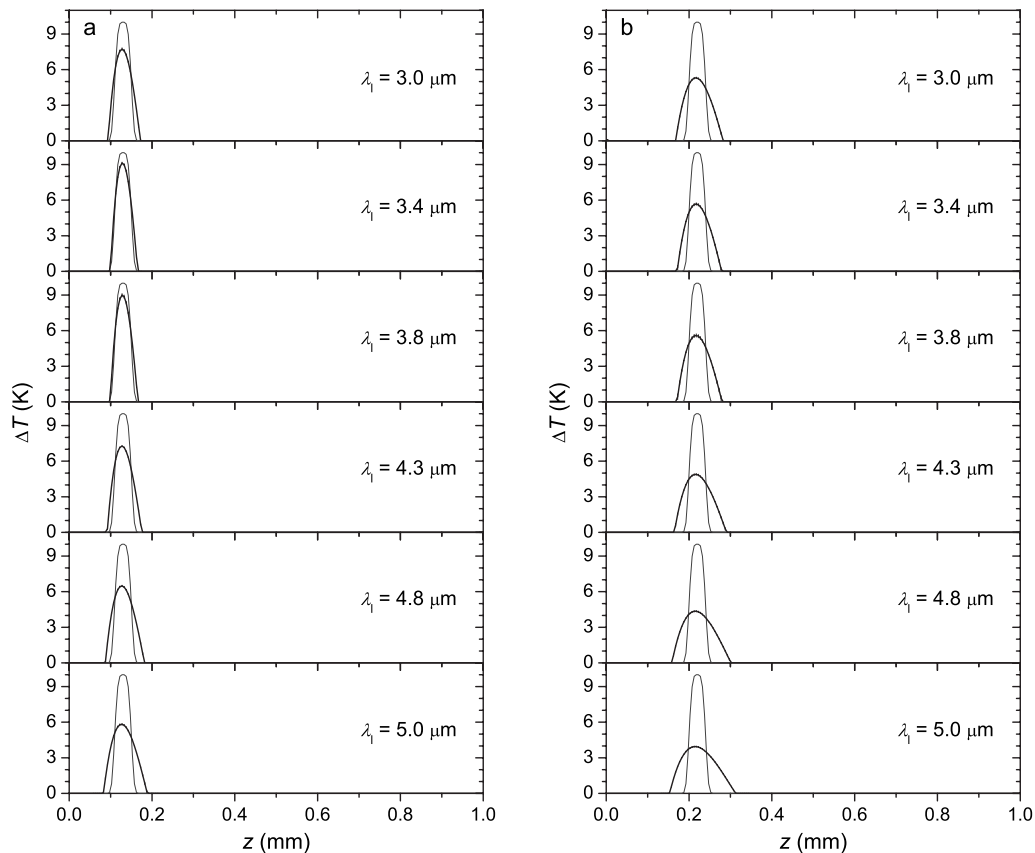
Fig. 7 Images of test objects (a) B with $z_0 = 0.13$ μm and (b) C with $z_0 = 0.22$ μm, reconstructed from simulated PPTR signals for spectral bands with λ_1 from 3.0 to 5.6 μm. Black lines are average results from 30 repetitions with different noise realizations; vertical bars indicate standard deviations. The assumed temperature profiles are plotted for comparison (thinner lines).
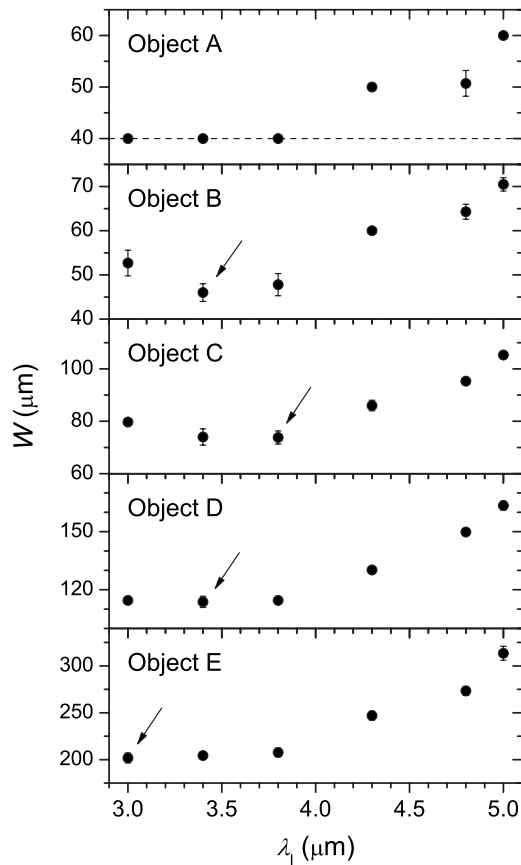
Fig. 8 Full width at half maximum (W) of the reconstructed temperature lobes as a function of the lower wavelength limit λ_l for test objects A–E (see the labels). Dashed line indicates the actual object width, vertical bars are standard deviations, and arrows mark minimal values in each data set.

Fig. 9 Relative image error (δ) as a function of λ_l for test objects A–E. Standard deviations are smaller than the symbol size. Arrows mark minimal values in each data set.

4.3 Port Wine Stain Lesion

In order to analyze the performance of PPTR temperature profiling utilizing different spectral acquisition bands in case of more complex geometries, we consider a temperature profile as obtained from Monte Carlo simulation of photon transport in a port wine stain (PWS) lesion.[15] Because this temperature profile extends somewhat deeper into the skin, the simulated PPTR signals correspond to an acquisition time of 2 s.

Figure 10 presents a comparison of simulation results obtained for six spectral bands. Reconstructed temperature values in the first peak ($z=0–50\ \mu$m) match the actual values somewhat better for spectral bands with $\lambda_l=3.4$ and 3.8 μm than for the broadest spectral band ($\lambda_l=3.0\ \mu$m). On the other hand, reconstruction of the first dip ($z=60\ \mu$m) and the second peak (100 μm) appear more accurate with $\lambda_l=3.0–3.8\ \mu$m as compared to the narrower spectral bands. Differences between the temperature profiles at depths below 0.5 mm are not significant.

Relative image errors δ for all spectral bands are compared in Fig. 11. The minimal error ($\delta=0.179$) is obtained for $\lambda_l=3.8\ \mu$m. The values for somewhat broader ($\lambda_l=3.4\ \mu$m) and narrower spectral bands ($\lambda_l=4.3\ \mu$m) are slightly larger, with the latter also featuring the smallest standard deviation

overall. These results agree quite well with numerical simulation of the collagen gel samples (Fig. 9).

5 Discussion

The depths of peak temperature as reconstructed from PPTR measurements in collagen gel samples using different spectral acquisition bands are very similar (Fig. 4). For all samples, the difference is smaller than the applied spatial discretization ($\Delta z=5\ \mu$m). This is supported by our numerical results, where selection of the spectral band does not significantly influence the accuracy of peak temperature depth determination. In the latter results, reconstructed peak temperature depths never deviate from the actual object depth z_0 by more than $\Delta z/2$. Note that the accuracy of PPTR determined absorbing layer depth was verified earlier using histology,[16] optical coherence tomography,[16] and high-resolution magnetic resonance imaging[12] in agar tissue phantoms.

It is well known that resolution of PPTR temperature profiling is limited by broadening of isolated temperature peaks, which increases with object depth.[3,6,9,12] This effect arises primarily from ill-posedness of the reconstruction problem and relatively high noise levels in IR radiation detection at the required sampling rates. Nevertheless, our results demonstrate that appropriate spectral filtering reduces the widths of reconstructed temperature profiles in samples C and D (Figs. 4 and 5), despite the associated decrease of SNR (Fig. 6). Tempera-
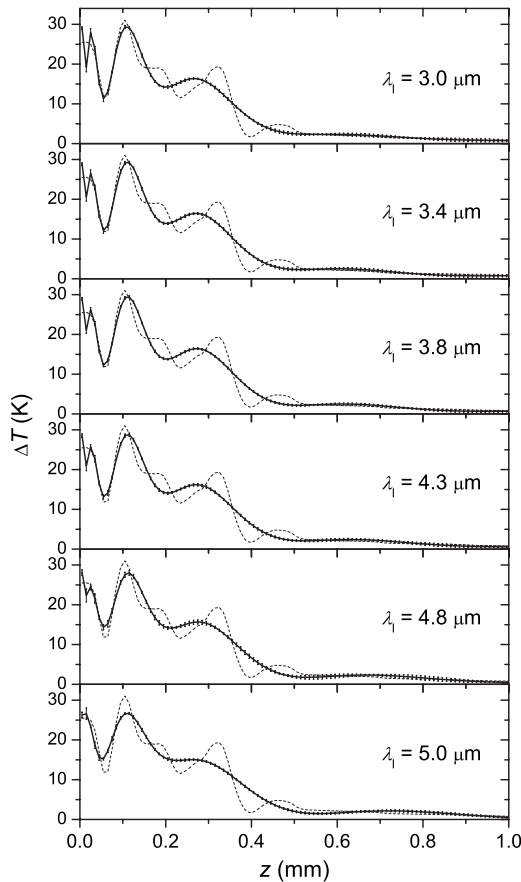
Fig. 10 Simulated profiling of PWS lesion using spectral bands with λ_l from 3.0 to 5.0 μm. Solid lines are average temperature profiles, and vertical bars are standard deviations from 30 repetitions with different noise realizations. The actual test object is plotted for comparison (dashed line).

ture profiles reconstructed from experimental PPTR signals with $\lambda = 3.8-5.6$ μm are narrower ($W = 105$ and 150 μm) as compared to the full-spectrum acquisition ($W = 110$ and 160 μm). The advantage of spectral filtering is not obvious for samples A, B, and E.

Similar trends are observed in our numerical results. For test objects B–D, the smallest differences between recon-
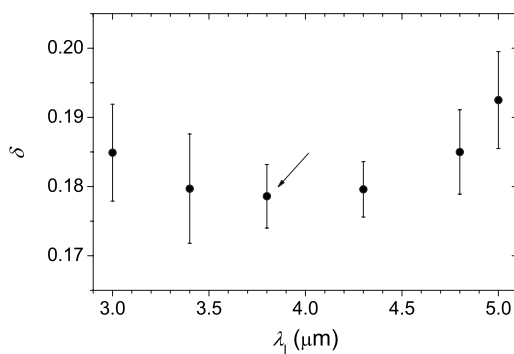
Fig. 11 Relative image error (δ) as a function of λ_l for the PWS test object. Error bars are standard deviations; arrow marks the minimal value.

structed widths W and the actual value are obtained for narrowed spectral bands with $\lambda_l = 3.4-3.8$ μm (Fig. 8). Relative reduction of width W with regard to using the full spectral band ($\lambda_l = 3.0$ μm) amounts up to 13% in test object B. The advantage of spectral filtering is not evident for objects A and E. Similarly, the relative image errors δ show distinct minimums at $\lambda_l = 3.8-4.0$ μm for objects A, B, and D (Fig. 9), whereas for test objects C and E, minimal δ is obtained for the broadest spectral band ($\lambda_l = 3.0$ μm).

Numerical simulation of PPTR profiling in PWS lesion supports the above observations. Spectral bands with $\lambda_l = 3.8$ μm result in minimal δ (Fig. 11), while $\lambda_l = 3.4$ or 4.3 μm yield comparable errors. This indicates that our findings are not limited to structures with single thin absorbing layers, but can be generalized to more complex temperature profiles, based on linearity of Eq. (3).

Clearly, the deficiency of monochromatic approximation is most expressed for the broadest, unfiltered acquisition spectral band, while adverse effects of noise dominate for narrow spectral bands. However, spectral filtering was not found to be as advantageous for collagen tissue phantoms as it was for agar gel.[9] This could be related to lower values of μ_{eff} (Fig. 6), due primarily to lower water content in the former, which makes the reconstruction problem somewhat more ill-posed. Our collagen gel, namely, mimics optical (IR) and thermal properties of human skin, so that the main conclusions (i.e., the benefit and optimal degree of spectral filtering) should be transferrable to PPTR profiling *in vivo*.

In general, structure of skin is certainly more complex than that of our phantoms. The demonstrated profiling technique is applicable only to specific situations where validity of one-dimensional approximation is ensured. One relevant example is PWS lesions, where both melanosomes in the epidermis and venules in papillary dermis are so numerous and small in comparison to the signal acquisition area that optical absorption can be considered laterally uniform. It remains to be seen to what extent our specific results (e.g., the extent of image broadening in relation to absorber depth and temperature rise) reflect performance of PPTR profiling of PWS *in vivo*. Nevertheless, currently available experimental evidence appears very promising.[3,11,17–19]

6 Conclusions

Appropriate spectral filtering can improve the accuracy of reconstructed temperature profiles in collagen-based tissues, despite the associated reduction of SNR. For the discussed PPTR system and samples, the results suggest application of long-pass filter with cut-on wavelength of $\lambda_l = 3.4-3.8$ μm. Because collagen gel closely resembles human skin in thermal, IR, and optical properties, we believe that these conclusions are directly transferrable to PPTR profiling of human skin *in vivo*.

References

1. F. H. Long, R. R. Anderson, and T. F. Deutsch, "Pulsed photothermal radiometry for depth profiling of layered media," *Appl. Phys. Lett.* **51**, 2076–2078 (1987).
2. S. L. Jacques, J. S. Nelson, W. H. Wright, and T. E. Milner, "Pulsed photothermal radiometry of portwine-stain lesions," *Appl. Opt.* **32**, 2439–2446 (1993).
3. T. E. Milner, D. M. Goodman, B. S. Tanenbaum, and J. S. Nelson,

"Depth profiling of laser-heated chromophores in biological tissues by pulsed photothermal radiometry," *J. Opt. Soc. Am. A* **12**, 1479–1488 (1995).

4. M. J. C. van Gemert, J. S. Nelson, T. E. Milner, D. J. Smithies, W. Verkruysse, J. F. de Boer, G. W. Lucassen, D. M. Goodman, B. S. Tanenbaum, L. T. Norvang, and L. O. Svaasand, "Non-invasive determination of port wine stain anatomy and physiology for optimal laser treatment strategies," *Phys. Med. Biol.* **42**, 937–950 (1997).

5. W. Verkruysse, B. Majaron, B. S. Tanenbaum, and J. S. Nelson, "Optimal cryogen spray cooling parameters for pulsed laser treatment of port wine stains," *Lasers Surg. Med.* **27**, 165–170 (2000).

6. U. S. Sathyam and S. A. Prahl, "Limitations in measurement of subsurface temperatures using pulsed photothermal radiometry," *J. Biomed. Opt.* **2**, 251–261 (1997).

7. M. Milanič, "Development and evaluation of pulsed photothermal radiometry for temperature profiling in biological tissues," Ph.D. thesis, University of Ljubljana (2008).

8. D. J. Smithies, T. E. Milner, B. S. Tanenbaum, D. M. Goodman, and J. S. Nelson, "Accuracy of subsurface distributions computed from pulsed photothermal radiometry," *Phys. Med. Biol.* **43**, 2453–2463 (1998).

9. M. Milanič, B. Majaron, and J. S. Nelson, "Spectral filtering for improved pulsed photothermal temperature profiling in agar tissue phantoms," *J. Biomed. Opt.* **13**, 251–261 (2008).

10. B. Majaron and M. Milanič, "Effective infrared absorption coefficient for photothermal radiometric measurements in biological tissues," *Phys. Med. Biol.* **53**, 255–268 (2008).

11. B. Majaron, W. Verkruysse, B. S. Tanenbaum, T. E. Milner, and J. S. Nelson, "Spectral variation of infrared absorption coefficient in pulsed photothermal profiling of biological samples," *Phys. Med. Biol.* **47**, 1929–1946 (2002).

12. M. Milanič, I. Serša, and B. Majaron, "Spectrally composite reconstruction approach for improved resolution of pulsed photothermal temperature profiling in water-based samples," *Phys. Med. Biol.* **54**, 2829–2844 (2009).

13. M. Born and E. Wolf, *Principles of Optics*, Pergamon Press, Oxford (1986).

14. J. D. Vincent, *Fundamentals of Infrared Detector Operation and Testing*, Wiley, Hoboken, NJ (1989).

15. B. Choi, B. Majaron, and J. S. Nelson, "Computational model to evaluate port wine stain depth profiling using pulsed photothermal radiometry," *J. Biomed. Opt.* **9**, 299–307 (2004).

16. M. Milanič, B. Majaron, and J. S. Nelson, "Pulsed photothermal temperature profiling of agar tissue phantoms," *Lasers Med. Sci.* **22**, 279–284 (2007).

17. T. E. Milner, D. J. Smithies, D. M. Goodman, A. Lau, and J. S. Nelson, "Depth determination of chromophores in human skin by pulsed photothermal radiometry," *Appl. Opt.* **35**, 3379–3385 (1996).

18. B. Li, B. Majaron, J. A. Viator, T. E. Milner, Z. Chen, Y. Zhao, H. Ren, and J. S. Nelson, "Accurate measurement of blood vessel depth in port wine stained human skin *in vivo* using pulsed photothermal radiometry," *J. Biomed. Opt.* **9**, 961–966 (2004).

19. B. Majaron, M. Milanič, and J. S. Nelson, "Interaction of a dual-wavelength laser system with cutaneous blood vessels," *Proc. SPIE* **6632**, 66320C (2007).